

## Article

# Local Effects in EHL Contacts with Oil-Impregnated Sintered Materials

Martin Ebner <sup>1,\*</sup> , Milan Omasta <sup>2</sup> , Thomas Lohner <sup>1</sup> , Petr Šperka <sup>2</sup> , Ivan Krupka <sup>2</sup> ,  
Martin Hartl <sup>2</sup>, Klaus Michaelis <sup>1</sup>, Bernd-Robert Höhn <sup>1</sup> and Karsten Stahl <sup>1</sup> 

<sup>1</sup> Gear Research Centre (FZG), Technical University of Munich (TUM), Boltzmannstraße 15, 85748 Garching near Munich, Germany; lohner@fzg.mw.tum.de (T.L.); michaelis@fzg.mw.tum.de (K.M.); hoehn@fzg.mw.tum.de (B.-R.H.); stahl@fzg.mw.tum.de (K.S.)

<sup>2</sup> Faculty of Mechanical Engineering, Brno University of Technology, Technická 2896/2, 616 69 Brno, Czech Republic; omasta@fme.vutbr.cz (M.O.); sperka@fme.vutbr.cz (P.Š.); krupka@fme.vutbr.cz (I.K.); hartl@fme.vutbr.cz (M.H.)

\* Correspondence: ebner@fzg.mw.tum.de; +49-89-289-15817

Received: 9 October 2018; Accepted: 6 December 2018; Published: 24 December 2018



**Abstract:** Oil-impregnated open-pored sintered materials can be used to provide the intrinsic self-lubrication of tribological contacts. Although its general functionality was recently confirmed for highly-loaded contacts, detailed analyses on the local effects of surface porosity in tribological contacts are required in order to understand and improve its operating behavior. In this context, this study investigates the influence of different surface finishes at a twin-disk test rig, and the local effects of surface porosity in elastohydrodynamically lubricated (EHL) contacts at an optical tribometer, based on thin film colorimetric interferometry. The results show the detrimental influence of high surface porosity on the operating behavior. Local observations of the lubricant film in EHL contacts indicate the presence of “open” pores, resulting in local film breakdown, and “closed” pores, transporting the additional lubricant into the pressurized zone. An appropriate surface finish technique to manufacture a low permeable layer with an adequate mechanical strength is demanded.

**Keywords:** EHL; oil film thickness measurement; optical measurement; sintered material; intrinsic lubrication; self-lubrication

## 1. Introduction

Sintered steel parts are well-known for the economic manufacturing of complex shapes, and are widely used in transmission systems. Within the manufacturing process of conventional powder metallurgy (PM), material porosity is adjusted by varying the density of the sintered steel, which influences the mechanical properties significantly. A density between 7.1 and 7.2 g/cm<sup>3</sup> is assumed as the transition area from an open to closed porosity (Dizdar [1], Lipp [2]). The term open porosity refers to the pores on the surface directly connected to the porous bulk material, so that the open pores can be used as transport channels (Dlapka et al. [3]). Sintered material with an open porosity can be impregnated with lubricant in order to provide intrinsic self-lubrication.

In lightly-loaded sintered journal bearings, the porosity of the sintered material has been already exploited for self-lubrication for many years. Kaneko and Obara [4] experimentally investigated the lubrication mechanism of porous journal bearings with a simplified test bearing. Using a dye-injection method, they observed that in a hydrodynamic lubrication regime, the oil in the porous matrix flows away from the loaded towards the unloaded zone. Pahl and Goller [5], and Bartz and Rübenbach [6] give an overview of the friction behavior, common materials, and lubricants for sintered journal bearings. Matzner et al. [7] analyzed the influence of various parameters,

including the permeability on the load-carrying capacity of the sintered journal bearings. They found that because of a lack of knowledge about the relationship between the manufacturing parameters and material permeability, the significant influence of the lubricant transport to the loaded contact zone on the operating behavior can be roughly approximated. Morgan and Cameron [8] were one of the first to calculate the lubricant circulation from the loaded to the unloaded zone in the porous journal bearings. Balasoiu et al. [9] calculated the oil flow in the porous journal bearings in detail. They confirmed the presence of lubricant-circulation, and found a decreasing load-carrying capacity with an increasing permeability. Also, Scheichl et al. [10] conducted simulations on the oil flow in sintered journal bearings, and showed that oil bleeds primarily in unloaded zones next to the loaded contact zone. Zhang et al. [11] investigated the effect of the porous surfaces of multilayer journal bearings on the lubrication, and recommend a low permeable surface.

Further studies on oil-impregnated sintered materials not related to journal bearings have been performed. Fote et al. [12] and Marchetti et al. [13,14] studied self-lubricating sintered materials for space applications. They found that the bleeding of the lubricant is mainly caused by capillary effects due to the surface roughness, different thermal expansion of porous material, and lubricant, as well as to centrifugal forces. Li, Sosa, and Oloffson [15] compared the tribological behavior of wrought and sintered steels by using a pin-on-disk test rig. They described an improved wear resistance of sintered parts with an open porosity because of an improved lubrication. In a more recent study, Li and Oloffson [16] found a correlation between the pore size, friction coefficient, and wear coefficient, and described peeling as one of the main failure modes.

The surface pores of oil-impregnated sintered materials led to the local phenomena in the tribological contacts. For elastohydrodynamically-lubricated (EHL) contacts, the effect of pores on the surface, which are not connected to the pore network in the sintered material (i.e., “closed” pores), may be compared to the effect of surface indentation. Its local effect on the lubricant film thickness in rolling-sliding point contacts was studied in detail by several researchers. Wedeven and Cusano [17,18] provided the first experimental evidence of film thickness variations around the indentation and implication to pressure distribution. Kaneta et al. [19,20] described a film thickness reduction in the vicinity of an indentation when it enters the edge of the central contact zone. Mourier et al. [21,22] showed, with numerical simulation and experiments, that the deep dents lead to a film reduction and breakdown, while the shallow dents increase the lubricant film thickness. Krupka et al. [23] further described the effect of the shallow dent geometry and conditions. Furthermore, they focused on the mixed lubrication regime [24] and start-stop and reversal motion [25].

Research on sintered gears has mainly been aimed at improving the mechanical properties and load-carrying capacity by densification of the tribologically stressed flank surfaces. The corresponding studies are based on conventional dip- or injection-lubrication. Frech et al. [26] investigated the cold rolling process for surface densification. They evaluated the influence of the process parameters on the density depth profile of sintered gears. Dizdar [1] reviewed various investigations on the pitting resistance of sintered small-module gears, and showed that the highest pitting resistance was for the manufacturing steps pressing, sintering, surface densification, and case-carburizing. Sandner et al. [27] performed experiments at a three-shaft gear test rig. They showed that sintered gears with a subsequent surface densification process can bear loads in the order of magnitude of wrought steel gears. Yoshida et al. [28] compared the surface durability of induction-hardened sintered gears with induction-hardened melted steel gears at a power circulating gear test rig. The surface durability was shown to be lower for the sintered gears. Pitting and spalling were observed as the main failure modes.

Ebner et al. [29] were the first to study the self-lubrication of oil-impregnated sintered materials in highly-loaded contacts. They confirmed its general functionality using experimental investigations at a twin-disk test rig and an efficiency gear test rig [30]. Different operating behaviors were correlated to the surface porosity of the test specimens at the end of the experiments. In Omasta et al. [31],

the authors confirmed lubricant film formation in EHL contacts with oil-impregnated sintered materials by observing the film thickness using optical interferometry. The findings show that starvation is likely to occur, the lubricant film thickness is mainly governed by the oil bleeding capacity, and the oil starvation parameters correlate well with the classic starved EHL theory.

The literature review shows that a lot of research has been performed on the self-lubricating mechanism of oil-impregnated sintered journal bearings. Experimental investigations on sintered gears have been focused on the densification of the flank surface and external lubrication. However, no systematic investigations on the self-lubrication of oil-impregnated sintered materials in highly-loaded contacts (e.g., gears) have been conducted. The first investigations of the authors [29] show that detailed analyses on the local effects of surface porosity in tribological contacts are necessary in order to understand and improve the operating behavior of self-lubricating sintered materials for highly-loaded applications. This has been addressed in this study by considering the various surface finishes with different surface porosities. Their operating behaviors are investigated by endurance measurements using a twin-disk test rig. The local effects of the surface pores in the highly-loaded EHL contacts are investigated using the optical film thickness measurements by means of thin film colorimetric interferometry.

## 2. Experimental Setups

The experimental setups of the twin-disk test rig and optical tribometer, as well as the considered materials, operating condition, and lubrication, are presented in the following sections.

### 2.1. Twin-Disk Test Rig

A FZG twin-disk test rig was used to investigate the influence of various surface finishes on the operating behavior of highly-loaded contacts with oil-impregnated sintered material.

#### 2.1.1. Mechanical Setup

Figure 1 shows the mechanical layout of the FZG twin-disk test rig according to Michaelis [32]. The following description of the test rig is based on the work and formulations of Lohner et al. [33] and Ebner et al. [29,34].

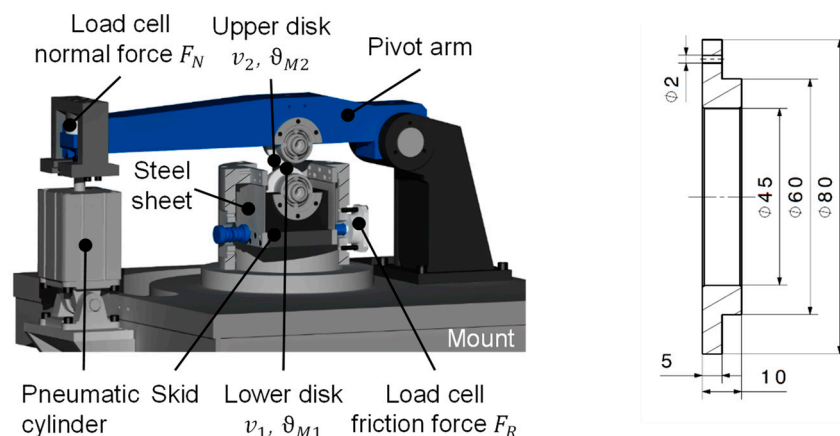


**Figure 1.** Mechanical layout of the FZG twin-disk test rig (Ebner et al. [35]) (left) and geometry of test disk (right).

The upper and lower disk were press-fitted onto shafts, which were individually rotated by two speed-controlled electric motors. This allowed for the continuous variation of the surface velocities,  $v_1$  and  $v_2$ , of the disks. The normal force,  $F_N$ , in the contact was continuously applied by a pneumatic cylinder via a pivot arm, where the upper disk was mounted. The lower disk was mounted in a skid, which was attached to the frame by thin steel sheets. The skid was supported laterally by a load cell,

so that the friction force,  $F_R$ , in the disk contact for sliding velocities,  $v_g \neq 0$  m/s, could be measured as a reaction force, with hardly any skid displacement. The normal force,  $F_N$ , friction force,  $F_R$ , and surface velocities,  $v_1$  and  $v_2$ , were measured. Additionally, the bulk temperature of the upper disk,  $\vartheta_{M2}$ , was measured 5 mm below the disk surface using a Pt100 resistance temperature sensor.

The sum velocity,  $v_\Sigma$ , and sliding velocity,  $v_g$ , are defined as follows:

$$v_\Sigma = v_1 + v_2 \quad (1)$$

$$v_g = v_1 - v_2 \quad (2)$$

The coefficient of friction,  $\mu$ , is obtained by the following:

$$\mu = \frac{F_R}{F_N} \quad (3)$$

All of the experiments at the FZG twin-disk test rig were conducted using cylindrical disks with a diameter of  $D = 80$  mm and a width of  $l_{eff} = 5$  mm (Figure 1, right). Hence, a line contact was formed. To ensure an evenly distributed load over the disk width of 5 mm, a contact print on aluminum foil was evaluated before each test, and any misalignment was carefully corrected mechanically.

### 2.1.2. Test Disks

In accordance with the configuration in Figure 1, the upper disk was made of the sintered steel Sint-D31 (Miba [36], DIN30910-4 [37]) with a volume-based porosity of about  $\Theta = 10\%$ , whereas the lower disk was made of solid steel 16MnCr5 (Deutsche Edelstahlwerke [38]). Table 1 summarizes the corresponding material properties and shows the much smaller Young's modulus of Sint-D31 compared to solid steel. Both of the disks were case-hardened, with a target case-hardening depth of  $CHD_{550HV1} = 0.8 + 0.2$  mm and a target surface hardness of 690–740 HV1. Note that the case hardening depth of the sintered disk was  $CHD_{550HV1} > 1.0$  mm, because of the open porosity.

**Table 1.** Material properties of test disks for the twin-disk test rig.

Material	Upper Disk	Lower Disk
	Sintered Sint-D31	Solid 16MnCr5
Young's modulus $E$ in N/mm <sup>2</sup>	130,000	210,000
Poisson ratio $\nu$	0.27	0.30
Density $\rho$ in g/cm <sup>3</sup>	7.00	7.76
Porosity $\Theta$ in %	$\approx 10$	-

Figure 2 illustrates the manufacturing process of a test disk made from sintered steel. Circular blanks were conventionally sintered to a near-net-shape and were post-processed. After the soft turning and case carburizing, the test disks were hard turned and ground to the geometry in Figure 1 (right). Three surface finishes, including longitudinally-ground with  $Ra \sim 0.15$   $\mu$ m, mechanically-polished with  $Ra \sim 0.01$   $\mu$ m, and etch-polished, were considered. The surface conditions of the sintered disks are documented in detail in Section 3.2.



**Figure 2.** Manufacturing process of sintered test disks.



In order to avoid the roughness influences from the solid steel disk as much as possible, it was mechanically polished to an arithmetic mean roughness of  $Ra < 0.01 \mu\text{m}$ .

All of the roughness measurements were determined using the profile method with a measurement length of  $L_t = 4 \text{ mm}$  and a cut-off wavelength of  $\lambda_c = 0.8 \text{ mm}$  for the longitudinally ground surfaces, and  $\lambda_c = 0.08 \text{ mm}$  for the polished surfaces. All of the roughness parameters were given as mean values of three measurement points evenly distributed over the circumference. For the etch-polished surface, the roughness measurement was left out, as it was not meaningful because of the high surface porosity and its influence on the measurement.

### 2.1.3. Operating Condition

The operating condition considered was in accordance with previous investigations [29,34], and is summarized in Table 2. The kinematics corresponded to the lower solid disk faster than the upper sintered disk ( $v_g > 0 \text{ m/s}$  with  $v_1 > v_2$ ).

**Table 2.** Considered operating condition for twin-disk test rig [29].

Parameter	Value
Normal force $F_N$ in N	3920
Sum velocity $v_\Sigma$ in m/s	4.0
Sliding velocity $v_g$ in m/s	0.4
Hertzian pressure $p_H$ in $\text{N/mm}^2$	1043

The operating condition was kept constant for each surface finish of the sintered disk paired with the polished solid steel disk. The designations for the disk pairings were ground-polished, polished-polished, and etched-polished.

## 2.2. Optical Tribometer

The local effects of the porosity on the lubricant film thickness in highly-loaded EHL contacts were investigated using an optical tribometer based on thin film colorimetric interferometry.

### 2.2.1. Mechanical Setup and Measurement Technique

Figure 3 shows the mechanical layout of the optical tribometer according to Omasta et al. [31]. In the tribometer, a transparent disk made from BK7 glass is loaded using a dead-weight lever mechanism against a cylindrical sintered disk. Both of the disks were separately driven by two speed-controlled electric motors, which allowed continuous variation of the sum and sliding velocity. The definitions of the sum velocity,  $v_\Sigma$ , and sliding velocity,  $v_g$ , are in accordance with the twin-disk test rig (Equations (1) and (2)).

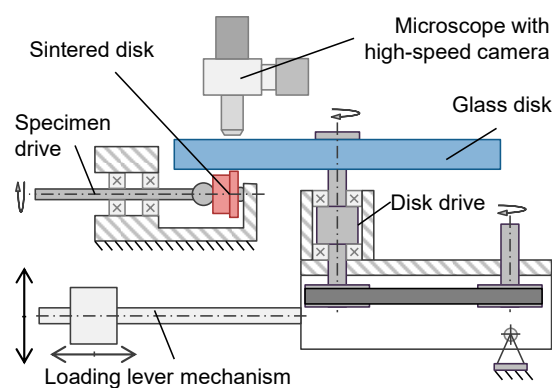


**Figure 3.** Mechanical layout of the optical tribometer.

The glass disk was equipped with a thin chromium layer on the contact side, with the sintered disk that allowed for an optical interference to occur. The contact was observed through an industrial microscope and was illuminated episodically with a high-intensity xenon continuous lamp. The resulting color interferograms were recorded using a high-speed CMOS camera with a frame rate of 8000 fps. The lubricant film thickness was evaluated using the thin film colorimetric interferometry technique [39]. An optical interference is a physical effect that occurs when two light beams reflected from nearby interfaces are composed together. In the case of the disk-on-disk optical tribometer, the first interface was between the thin chromium layer deposited on the glass disk and the oil film, and the second interface was between the disk and the oil film. As a result, color interferograms occurred, where each color corresponds to a specific film thickness. The conversion to the lubricant film thickness was made using a color-matching algorithm and CIELAB color-film thickness calibration integrated in the ACHILES software.

### 2.2.2. Test Disks

The sintered disk for the optical tribometer was cylindrical, with a diameter of 25.4 mm and a running surface with a width of 2 mm (see Figure 4). The sintered disk was made from the sintered steel Sint-D31, with the same procedure as described in Section 2.1.2. To investigate the local influence of pores in EHL contacts in detail, the running surface was mechanically polished to an arithmetic mean roughness of  $Ra < 0.01 \mu\text{m}$ .

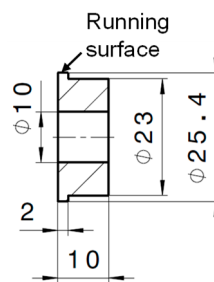


Figure 4. Geometry of the sintered disk for the optical tribometer.

### 2.2.3. Operating Condition

The local effects of the sintered material with a porous surface on the lubricant film thickness were evaluated under the operating conditions defined in Table 3. The maximum Hertzian pressure and sum velocity were lower compared to the FZG twin-disk test rig, with respect to the mechanical limits of the optical tribometer.

Table 3. Operating conditions for optical tribometer.

Parameter	Value
Normal force $F_N$ in N	241
Sum velocity $v_\Sigma$ in m/s	0.2
Sliding velocity $v_g$ in m/s	$\pm 0.1$
Hertzian pressure $p_H$ in $\text{N/mm}^2$	400

### 2.3. Lubrication

The sintered disks for the twin-disk test rig and optical tribometer were impregnated with oil in order to obtain self-lubrication.

In accordance with previous studies [29], the oils FVA3 and FVA3+PD were considered for the twin-disk test rig. FVA3 is an ISO VG 100 mineral oil [40], and FVA3+PD has the same base oil and a plastic deformation (PD) additive incorporated. Further information on FVA3+PD and its tribofilm characteristics can be found in Lohner et al. [33] and Emrich et al. [41]. In terms of self-lubrication with

oil-impregnated sintered materials, FVA3 provided a reference with a comparably large experimental basis [29], whereas FVA3+PD showed promising results on the operating behavior with low coefficients of friction [30].

For the disks for the optical tribometer, a lower viscosity oil FVA2 (ISO VG 32 mineral oil according to [40]) was used instead of FVA3, as a result of technological issues of the impregnation device.

The oil was impregnated by pressurization from the bore in radial direction, until oil bleeding was detected on the running surface of the disks. For the sintered disk for the twin-disk test rig, Figure 5 exemplifies that the average weight gain is  $\Delta m \sim 2.1$  g when impregnating FVA3 or FVA3+PD. This is consistent with the calculated weight gain based on the volume-based porosity of  $\sim 10\%$ .

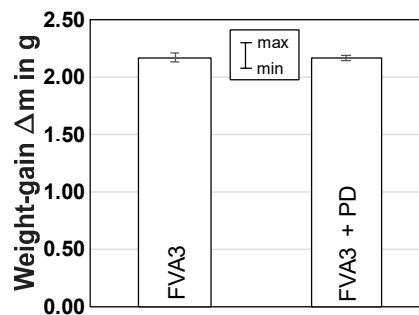


**Figure 5.** Weight-gain of sintered disks for the twin-disk test rig after impregnating FVA3 and FVA3+PD.

In order to press-fit the sintered disks onto the shaft of the twin-disk test rig, the shaft was cooled down in liquid nitrogen to avoid oil loss due to an increase of the bulk temperature. The test disks for the optical tribometer were mounted with a transition tolerance on the shaft, and were fixed in an axial direction.

For the self-lubrication on the twin-disk test rig, only the oil bleeding from the sintered disk was available for lubrication. In order to avoid dry lubrication during the first load cycles, the running surface of the solid steel disk of the twin-disk test rig was wetted with an initial lubricant volume of 0.02 mL before each test run. The same procedure was used in the tests on the optical tribometer, so as to avoid lubricant starvation.

### 3. Characterization of Sintered Samples

In terms of the sintered materials, a difference between the bulk and surface porosity depending on the surface finish is expected. Furthermore, Ebner et al. [29] found a correlation between the operating behavior and the surface porosity after experiments. In the following, the bulk porosity of a test disk from the twin-disk test rig is documented first, before the surface porosity is investigated in detail at the different manufacturing steps and for different finishing processes.

#### 3.1. Bulk Porosity

The light microscope picture of a cross-section of a sintered test disk in Figure 6 illustrates the pore distribution two-dimensionally.

To provide a visualization of the three-dimensional pore system inside the sintered material, a measurement using X-ray computed tomography ( $\mu$ CT) was carried out. The  $\mu$ CT scanning was made on a laboratory system GE Phoenix v|tome|x L 240 (GE Sensing and Inspection Technologies GmbH, Wunstorf, Germany) [42]. A cuboid part of the sintered disk, with an edge length of about 3 mm, with an etch-polished surface was prepared. The size of the sample allowed measurements with a spatial resolution of 3  $\mu$ m. Hence, pores with a size smaller than the resolution were not detected. As the  $\mu$ CT measurement digitized the porous material in all three of the space coordinates, the volume of the solid and of the pores could be evaluated. Especially when the data were measured with a

small voxel resolution [42], the evaluation generally provided lower values than those determined by the volumetric method. Nevertheless, the technique is suitable for the assessment of the pore size distribution.



**Figure 6.** Light microscope picture of bulk porosity of a sintered disk sample for the twin-disk test rig.

Figure 7 shows the captured cuboid sample by illustrating the solid volume (left) and the pore volume (right), while the graph in Figure 8 shows the number of pores over the pore volume. The results show that the pores form an open network that is very uniform in all directions, and is equally distributed over the sample. Under the assumption that the pores are depicted as spheres, the average pore diameter is approximately 14  $\mu\text{m}$ . This kind of a bulk porosity should allow for lubricant flow in the porous sample, which is the main prerequisite for the self-lubricating mechanism.

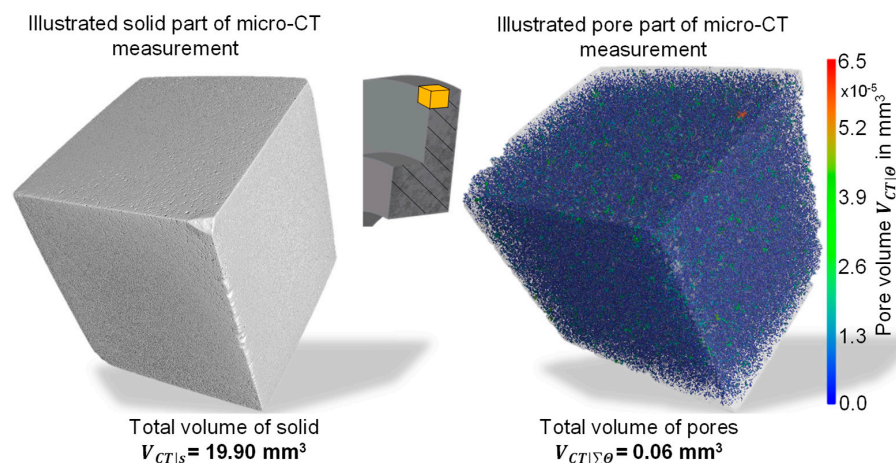


**Figure 7.** X-ray computed tomography ( $\mu\text{CT}$ ) measurement of bulk porosity of a cuboid sintered disk sample with an edge length of 3 mm.

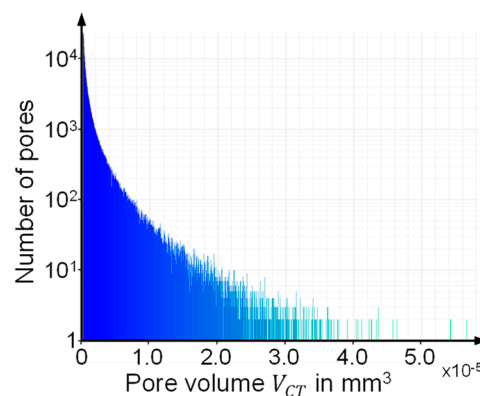


**Figure 8.** Number of pores over pore volume of a cuboid sintered disk sample evaluated from micro-CT measurement.

### 3.2. Surface Porosity

The change of surface porosity at different manufacturing steps and for different surface finishes is visualized by the representative light microscope pictures and scanning electron microscopy (SEM) images of the running surface in Figure 9. After sintering the circular blank at 1125 °C at a holding time >30 min under a N<sub>2</sub>/H<sub>2</sub> atmosphere, the porosity on the surface was clearly visible. The subsequent soft turning, hard turning, and grinding was done with the usual manufacturing parameters for steel machining. After soft turning and case carburizing at a temperature >900 °C with a holding time of >40 min under a N<sub>2</sub>/CH<sub>3</sub>OH atmosphere, the size and number of pores did not change significantly. After hard turning and longitudinal grinding, the machining direction was clearly apparent and the SEM images suggest smearing up the pores that lead to a lower number and size of pores on the surface.

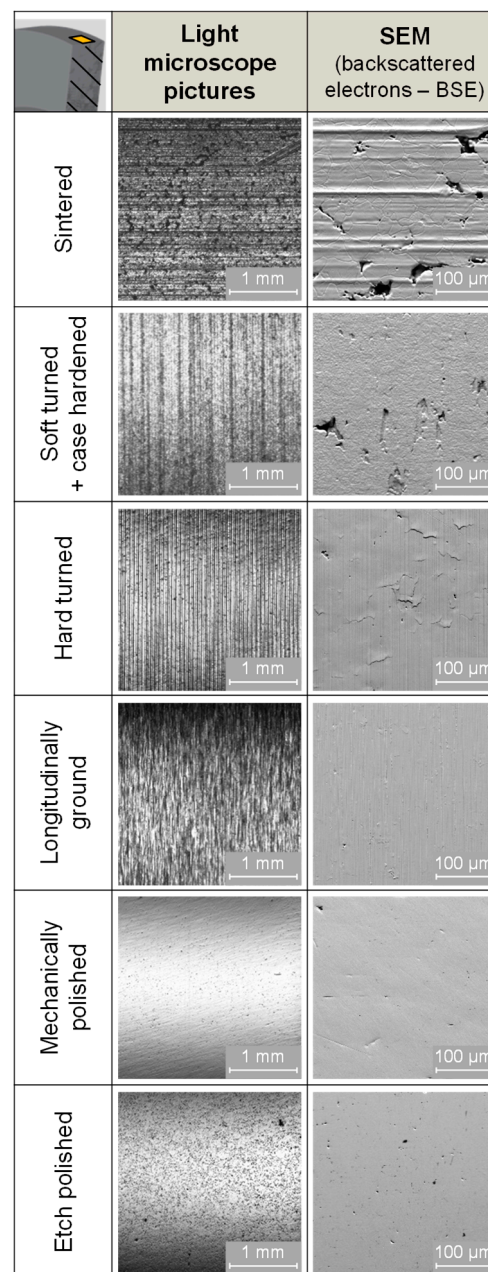


**Figure 9.** Influence of manufacturing steps and surface finishes on the surface porosity of a sintered test disk from the twin-disk test rig.



Mechanically polishing after grinding is a multi-stage process using an adapted grinding machine for metallographic grindings. Thereby, the ground surfaces are polished using a polishing cloth and a 3  $\mu\text{m}$  diamond suspension. Figure 9 shows that the polishing process tends to open smaller pores again. Etching with a 2% alcoholic nital etchant, and the subsequent polishing, results in a further increase of the surface porosity. Thereby, the number of pores is much higher and the size of the pores is much smaller compared to the original surface after sintering.

For the longitudinally ground and mechanically polished disk surface, the surface porosity was investigated by marking pores and counting their area during the image analysis. Around the disk circumference, eight evenly distributed images were recorded using SEM at  $200\times$  magnification. For the longitudinally ground and polished surface, the evaluated surface porosity was found to be  $\Theta_{sf} = 0.19\%$  and  $\Theta_{sf} = 0.30\%$ . Hence, the surface porosity after the surface treatment was significantly lower compared to the volume-based porosity of about  $\Theta = 10\%$ . A comparison between the corresponding SEM surface images in Figure 9 and the representative light microscope picture of the bulk porosity in Figure 6 clarifies the difference.

#### 4. Experimental Results

In this section, the experimental results from the twin-disk test rig on the influence of the different manufacturing steps and surface finishes are shown. This is supplemented by in-depth analyses on the local effects of the surface porosity in highly-loaded EHL contacts.

##### 4.1. Twin-Disk Test Rig

Figure 10 shows the measurement results of the coefficient of friction (top) and related bulk temperature (bottom) for the considered disk pairings at  $p_H = 1043 \text{ N/mm}^2$ ,  $v_\Sigma = 4.0 \text{ m/s}$  and  $v_g = 0.4 \text{ m/s}$ , in comparison with the lubricants FVA3 (left) and FVA3+PD (right). Information about the preparation of the samples are given in Sections 2.1.2 and 3.2. The results with the surface combination ground–polished are added to the results published previously [29].

All of the experiments with FVA3 and FVA3+PD showed a clear back coupling between the profile of the bulk temperature and the coefficient of friction. The tests were stopped because of high coefficients of friction ( $\mu > 0.12$ ) or high bulk temperatures  $\vartheta_{M2} > 150 \text{ }^\circ\text{C}$ . Furthermore, two tests with disk pairing ground–polished were stopped manually at 2.2-M and 0.65-M load cycles, and one test with disk pairing polished–polished was stopped manually after 0.64-M load cycles. The following description is separated into the investigated disk pairings.

With the impregnated oil FVA3, the disk pairing ground–polished shows stable (stationary), metastable (oscillating), and unstable (non-stationary) operating behaviors even at the same operating condition [29]. This could be correlated to the surface porosity after the test runs. Metastable and unstable operating behaviors show an increased number and size of pores on the running surface of the sintered disks after the test runs, whereas for the stable operating behaviors, the surface porosity of the sintered disk does not significantly change during the test run.

The PD-additive in FVA3+PD induces tribofilms that reduce the solid coefficient of friction, and, hence, the coefficient of friction in the mixed lubrication quite strongly (Emrich et al. [41], Lohner et al. [33]). Therefore, the good repeatability using FVA3+PD can be traced back to its specific tribofilm forming capability. However, after about 1-M and 1.5-M load cycles, the coefficient of friction and bulk temperature increase significantly, which is traced back to the exhaustion of the PD-additive (Ebner et al. [30]).

Also, for the disk pairing polished–polished and lubricant FVA3, only one out of the three test runs showed a stable operating behavior until the coefficient of friction increased, and the test run was stopped at 2.6-M load cycles. The two other test runs showed a metastable operating behavior and were stopped at 0.6-M and 0.5-M load cycles because of increasing coefficients of friction. However, no unstable operating behavior is observed for the disk pairing polished–polished.

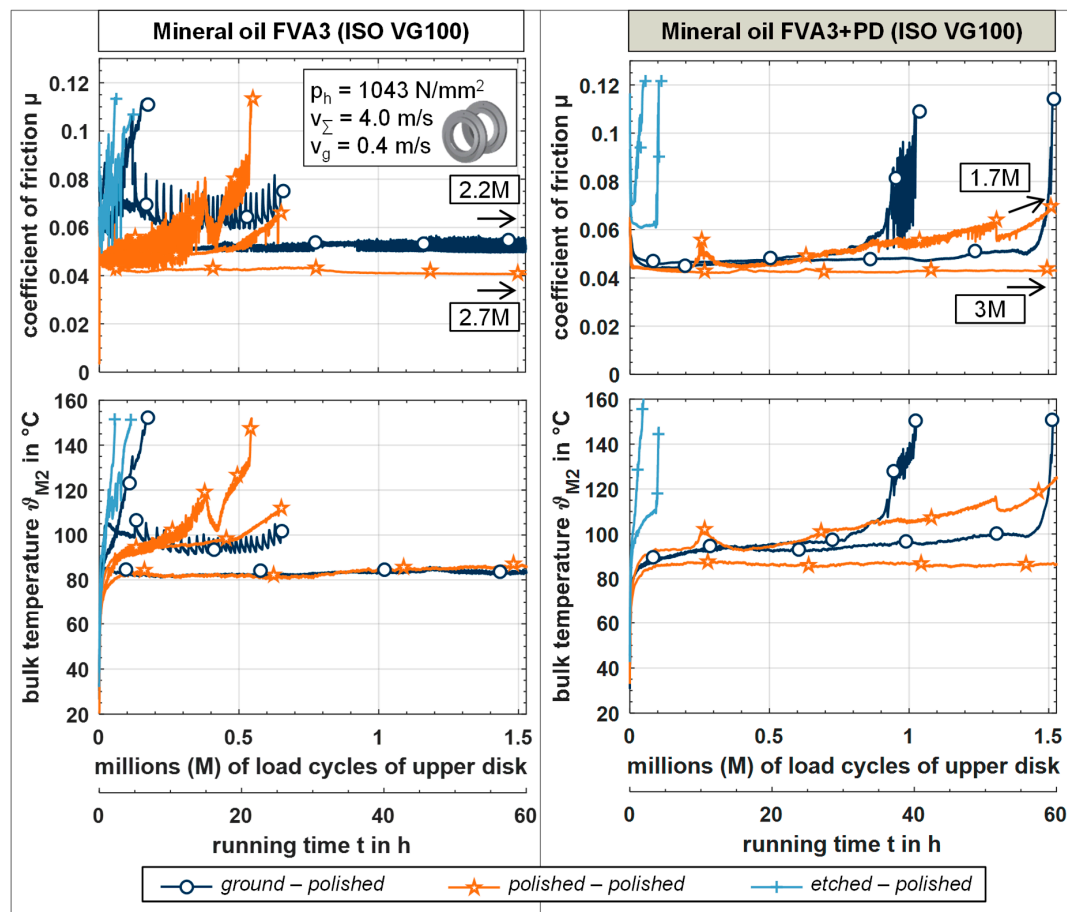


**Figure 10.** Measurement results of the coefficient of friction (**top**) and related bulk temperature (**bottom**) from the twin-disk test rig for different disk pairings at  $p_H = 1043 \text{ N/mm}^2$ ,  $v_\Sigma = 4.0 \text{ m/s}$ , and  $v_g = 0.4 \text{ m/s}$ , in comparison with lubricants FVA3 (**left**) and FVA3+PD (**right**).

For FVA3+PD, both test runs reached a stable operating behavior, until the likely the exhaustion of the PD-additive resulted in a metastable behavior. The test runs were stopped because of the bulk temperatures of  $\vartheta_{M2} > 50 \text{ }^\circ\text{C}$ . As the level of friction is higher for the test stopped at 1.7-M load cycles, the bulk temperature is also higher than for the test stopped at 3.0-M load cycles.

In contrast to the disk pairings of polished-polished and ground-polished, only unstable operating behaviors were observed with the disk pairing etched-polished for FVA3 and even for FVA3+PD. Thereby, all of the test runs were stopped after  $\leq 0.12\text{-M}$  load cycles, because of high coefficients of friction ( $\mu > 0.12$ ) and bulk temperatures ( $\vartheta_{M2} > 150 \text{ }^\circ\text{C}$ ).

#### 4.2. Optical Tribometer

A typical high-speed interferogram from the optical tribometer, under the conditions described in Table 2, is depicted in Figure 11. This is a part of the EHL line contact with a window size of  $850 \mu\text{m} \times 500 \mu\text{m}$ , and the image exposition of  $125 \mu\text{s}$ . Each color in the contact area corresponds to a defined lubricant film thickness. An approximate scale is shown below the interferogram. The surfaces move in the gap length direction. The cavitation in the exit of the contact area is visible at the top of the interferogram. It is evident that the EHL lubricant film is significantly influenced by the porous surface features of the sintered disk. Several specific areas can be distinguished, as follows:

- Area A represents an area where the lubricant film thickness is almost not affected by the surface features. Hence, a uniform central film thickness of approximately  $90 \text{ nm}$  could be expected for the ideally smooth surfaces.

- A thicker lubricant film occurs in Area B thanks to the so-called complementary wave that is generated by a surface feature in the contact inlet. The complementary wave moves through the contact at the mean surface velocity under rolling–sliding conditions (Greenwood and Johnson [43]).
- Area C indicates an area with a local lubricant film breakdown. The lubricant film thickness in the light grey area approaches 0 nm.
- Finally, shallow depressions on the sintered surface can be identified by an increase in the local lubricant film thickness, as seen in Area D.

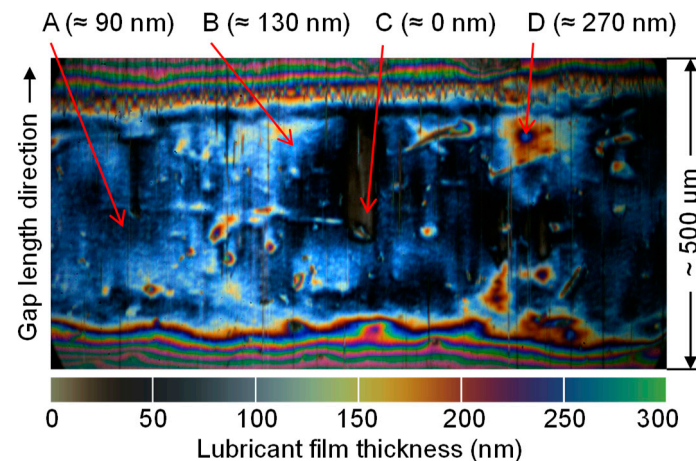


**Figure 11.** Typical interferogram from the optical tribometer with sintered disk at  $p_H = 400 \text{ N/mm}^2$ ,  $v_\Sigma = 0.2 \text{ m/s}$ , and  $v_g = 0.1 \text{ m/s}$  (surface velocity of sintered disk is lower).

The effects on the lubricant film thickness described by Figure 11 depend particularly on the sliding direction (i.e., whether the glass disk or the sintered disk has a higher velocity), and on the type of porous surface features. The surface of the glass disk is considered to be smooth, while the surface of the sintered disk contains local depressions (i.e., pores). With respect to mechanically polishing as its surface finish, it is supposed that there are no significant protrusions. Based on the experimental results, two types of pores can be identified, “open” pores with a connection to the porous bulk structure, and “closed” pores isolated as a kind of dimple at the surface.

In the following, four combinations of sliding direction and types of pore are described, through the observation of specific features in the sequences of high-speed interferograms from Figures 12–15. The time-step between the images is  $750 \mu\text{s}$  and  $250 \mu\text{s}$  when the surface of the sintered specimen is slower and faster, respectively. The size of each image of a sequence is  $10 \mu\text{m} \times 500 \mu\text{m}$ .

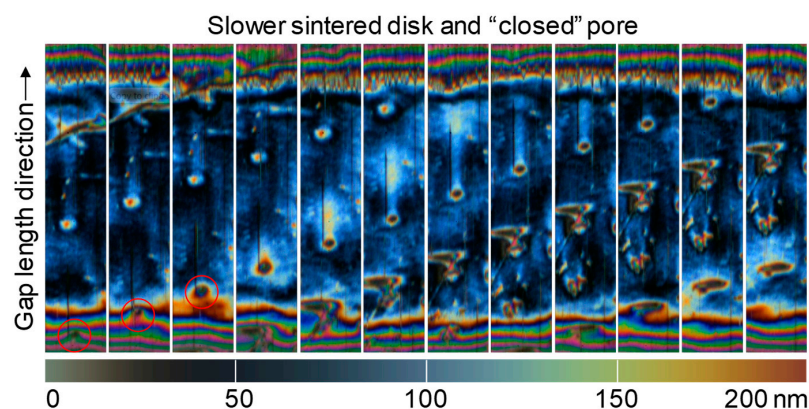


**Figure 12.** Sequence of interferograms from the optical tribometer showing the passage of a “closed” pore with lower surface velocity at  $p_H = 400 \text{ N/mm}^2$ ,  $v_\Sigma = 0.2 \text{ m/s}$ , and  $v_g = 0.1 \text{ m/s}$ .



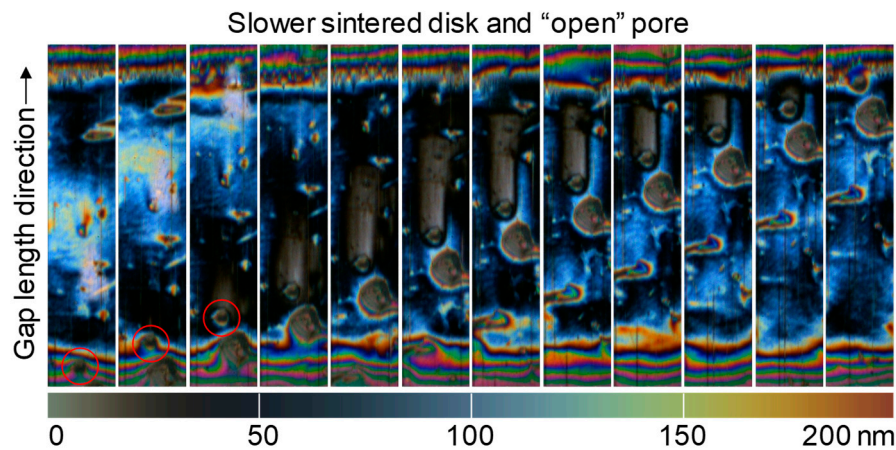


**Figure 13.** Sequence of interferograms from the optical tribometer showing the passage of an “open” pore with lower surface velocity at  $p_H = 400 \text{ N/mm}^2$ ,  $v_\Sigma = 0.2 \text{ m/s}$ ,  $v_g = 0.1 \text{ m/s}$ .

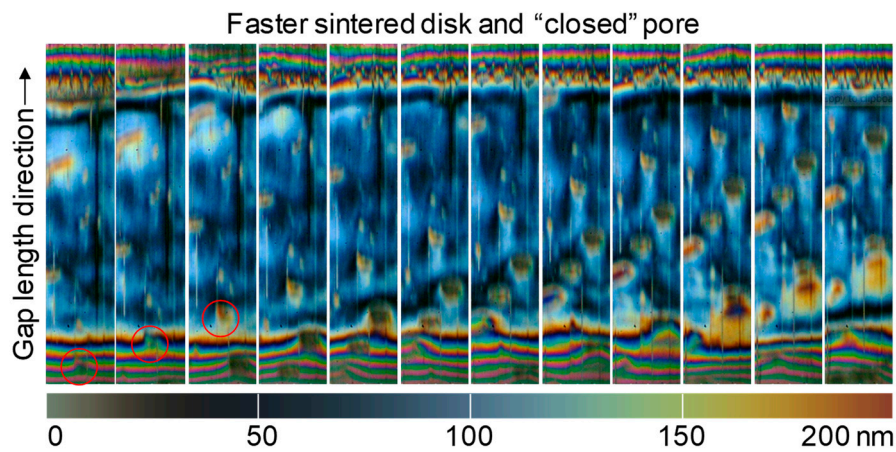


**Figure 14.** Sequence of interferograms from the optical tribometer showing the passage of a “closed” pore with higher surface velocity at  $p_H = 400 \text{ N/mm}^2$ ,  $v_\Sigma = 0.2 \text{ m/s}$ , and  $v_g = -0.1 \text{ m/s}$ .

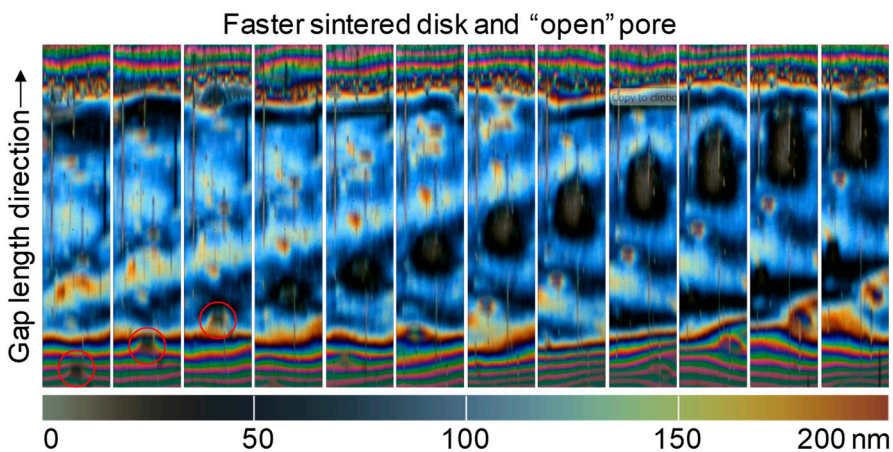


**Figure 15.** Optical tribometer: sequence of interferograms showing the passage of an “open” pore with higher surface velocity at  $p_H = 400 \text{ N/mm}^2$ ,  $v_\Sigma = 0.2 \text{ m/s}$ , and  $v_g = -0.1 \text{ m/s}$ .

#### 4.2.1. Slower Sintered Disk and “Closed” Pore

The movement of a “closed” pore with the sintered disk slower than the glass disk is marked in Figure 12. Once the pore enters contact, the lubricant starts to be emitted from the pore in the moving direction. This lubricant moves with the mean lubricant velocity, which is higher than the speed

of the pore, so the effect extends in gap length direction, while the film thickness at the pore decreases. This effect has a positive impact on the overall film thickness in the contact.

#### 4.2.2. Slower Sintered Disk and “Open” Pore

The effect of an “open” pore with the sintered disk moving slower than the glass disk is totally different, as shown in Figure 13. Once the pore enters the contact, it causes a steep lubricant film breakdown. Also, this effect acts in the gap length direction with the mean lubricant velocity. Thus, the area of the broken lubricant film gradually elongates in the gap length direction, while maintaining the width corresponding to the width of the pore. In Figure 13, there is another larger “closed” pore entering the contact after the described open one. Although a large amount of lubricant is released from this “closed” pore, there is no effect in the shade of the considered “open” pore.

#### 4.2.3. Faster Sintered Disk and “Closed” Pore

When the sintered disk has a higher velocity than the glass disk, the pores influence the lubricant film thickness opposite to the gap length direction. The “closed” pore marked in Figure 14 emits a lubricant that moves at the mean lubricant speed, which is lower than the velocity of the sintered disk. This effect is positive just behind the dimple, however, on the side, the lubricant film thickness decreases. So, with respect to the total change in lubricant film thickness, the effect is rather neutral.

#### 4.2.4. Faster Sintered Disk and “Open” Pore

When the sintered disk has a higher velocity than the glass disk, the effect of an “open” pore is negative, as can be seen from Figure 15. The marked pore causes lubricant film breakdown in its shadow against the movement in gap length direction. It is apparent that the lubricant is also exhausted from a wider neighborhood of the pore in all directions.

During the test runs at the optical tribometer, another observation was also made; although the running time of the test runs was short and there was no lubricant film breakdown because of oil starvation, an increasing number of pores on the surface of the sintered specimen was apparent. Figure 16 shows the interferograms of the EHL contact and corresponding light microscope images of the surface of one of the sintered disks at the beginning and after 15 and 60 min of testing. Surprisingly, there was almost no wear on the very thin chromium layer of the glass disk.

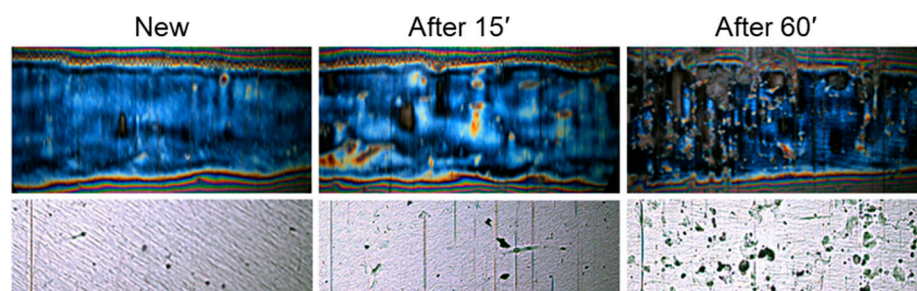


**Figure 16.** Interferograms from the optical tribometer of running contact and light microscope images of sintered disk after various times of testing.

## 5. Discussion

The experimental results from the twin-disk test rig in Section 4.1 showed, for the FVA3 and ground–polished disk pairings, unstable, metastable, and stable operating behaviors. For the polished–polished disk pairings, no unstable operating behavior was found. This may be mainly traced back to the much smaller surface roughness. However, for ground–polished and polished–polished disk pairings, the results with FVA3+PD showed very similar stable operating behaviors. The polished–polished disk pairings only reached a higher number of load cycles until the test runs were stopped because of the



high coefficients of friction. The more uniform occurrence of stable operating conditions with FVA3+PD are traced back to the PD-additive forming tribofilms in mixed lubrication regimes that reduce the solid coefficient of friction significantly (Emrich et al. [41]; Lohner et al. [33]). This “stabilizes” the operating behavior until the additive is exhausted. The higher number of load cycles of polished–polished disk pairings are likely due to the slower exhaustion of the PD-additive because of the lower surface roughness.

This indicates operation in mixed lubrication with solid contacts for all of the considered disk pairings and lubricants at the twin-disk test rig. Thereby, mixed lubrication is expected to be less pronounced for the disk pairing of polished–polished compared to ground–polished. All of the sintered disks show a surface porosity with a higher number and size of pores after reaching the abortion criteria, compared with the documentation before the test run. This is shown in Figure 17 by the representative SEM images of the sintered test disks, after the test runs at the twin-disk test rig stopped due to  $\vartheta_{M2} > 150\text{ }^{\circ}\text{C}$ . In comparison, Figure 9 shows the representative SEM images of the ground–, polished–, and etch–polished surfaces of the sintered disks before the tests. The change in surface porosity is seen as being responsible for the limited endurance of the polished–polished and ground–polished disk pairings. This correlates to the test results with the etched–polished disk pairings with a high number of pores even before the test run. In this case, all of the test runs show unstable operating behaviors with a very low number of load cycles for FVA3 and FVA3+PD.

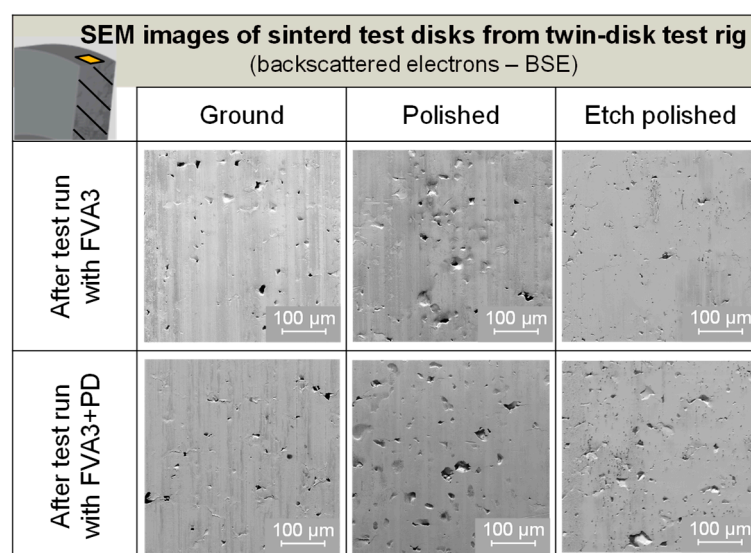


**Figure 17.** Representative SEM images of sintered test disks after test runs at the twin-disk test rig stopped due to  $\vartheta_{M2} > 150\text{ }^{\circ}\text{C}$  with FVA3 and FVA3+PD.

Although a higher surface porosity can support the bleeding of the lubricant, it also strongly affects the EHL lubricant film, as shown by the results from the optical tribometer. Too many “open” pores can cause too many local film thickness breakdowns, resulting in direct solid contacts and the continuous stress and wear of the surface. To understand this in more detail, the results for “open” and “closed” pores for different kinematic conditions in Section 4.2 are discussed in detail in the following.

Small “closed” pores can be interpreted as micro-dimples transiting through the contact. Therefore, a comparison with the effect of a single micro-dimple allows for a more precise description of the effect of “closed” pores on local lubricant film thickness. Figures 18 and 19 show the passage of a single micro-dimple through a circular EHL contact. The specific operating conditions of the test are described in the literature [25]. A dimple with a depth of 950 nm and a diameter of 45 µm was produced mechanically by a Rockwell indenter. Figure 18 clearly shows that if the dimpled surface is faster, a local film thickness depression is formed in the inlet zone, which then transits through the EHL contact, followed by a local film thickness increase. This is due to lubricant flow from the dimple.

With respect to the minimum film thickness, the effect is negative. If the dimpled surface is slower, as shown in Figure 19, a negative inlet effect does not occur. The minimum film thickness occurs just behind the dimple when leaving the EHL contact.

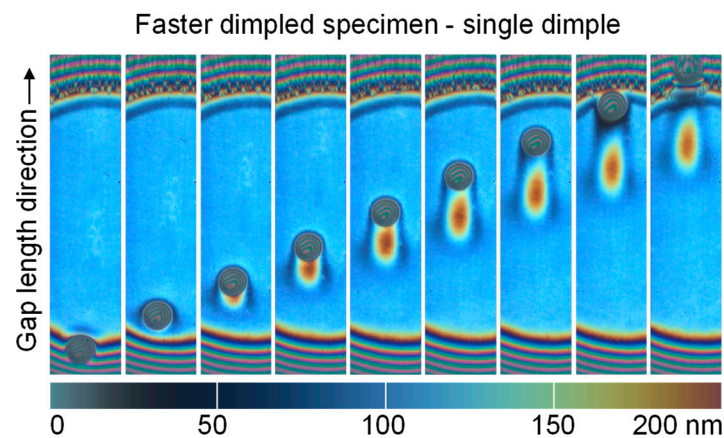


**Figure 18.** Sequence of interferograms from the optical tribometer showing the passage of a single dimple through a circular elastohydrodynamically lubricated (EHL) contact—faster dimpled surface.

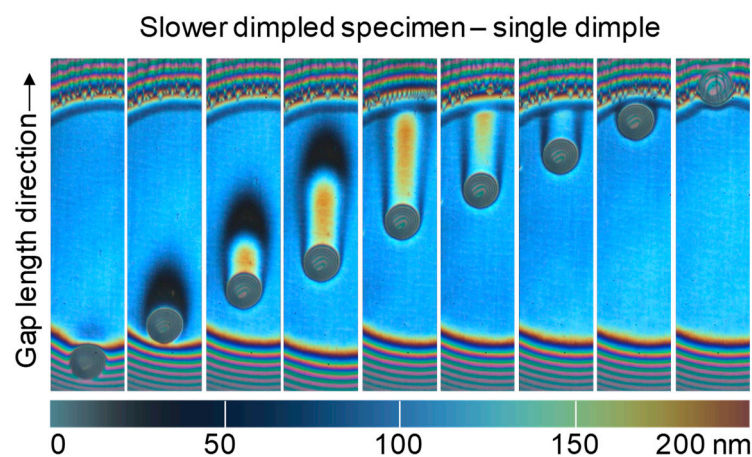


**Figure 19.** Sequence of interferograms from the optical tribometer showing the passage of a single dimple through a circular EHL contact—slower dimpled surface.

The quantitative variation of the lubricant film thickness at various cross-sections in comparison to a surface with and without micro-dimple is shown in Figure 20. If the dimpled surface is slower, the overall effect is negligible and the dimple causes only a redistribution of the lubricant in its vicinity. On the other hand, if the dimpled surface is faster, an overall film thickness increase occurs. Under these conditions, the average increase is approximately 10 nm in longitudinal direction. These conclusions on lubricant film thickness can also be qualitatively transferred to the local effect of a porous surface with “closed” pores.

There is also an important effect of the size of dimples, as indicated in Figure 21. For smaller dimples obtained by a smaller indentation depth, the negative inlet effect disappears when the dimpled surface moves slower.

As an analogy for “closed” pores, the discussion on the effect of micro-dimples on the EHL contact shows that “open” pores, which are connected to the porous bulk structure, are much more serious, as they cause local lubricant film breakdown, no matter which surface moves. The explanation relates to the pressure gradient occurring as a result of “open” pores. Once an “open” pore enters the EHL contact, high pressure forces the lubricant to flow into the “open” pore.

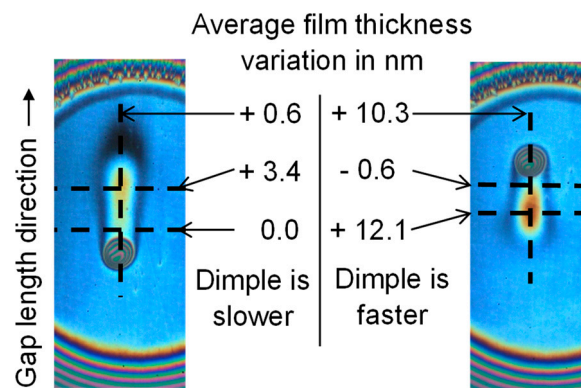


**Figure 20.** Quantitative comparison of average film thickness variation for a slower and faster dimpled surface at two gap length positions and one gap width position.

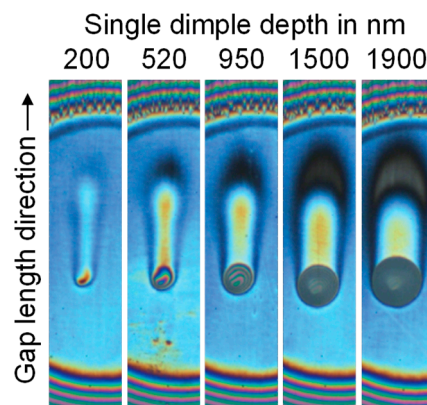


**Figure 21.** Qualitative comparison of average film thickness variation for different sizes of dimples.

Hence, exceeding a critical number of “open” pores is the main reason that sintered disks with a high surface porosity lead to unstable operating behavior at the twin-disk test rig. For etched–polished disk pairings, this critical number of “open” pores is already exceeded after the surface finish, hence, all of the test runs show an unstable operating condition.

The optimal number of “open” pores can be defined as enough “open” pores to provide lubricant flow for self-lubrication, but too little to affect the EHL lubricant film too much by local disturbances. This balance seems to be approached by ground–polished disk pairings because of the smearing-up of pores during grinding, which results in a much smaller surface porosity of only  $\Theta_{sf} = 0.19\%$ . However, it seems that the mechanical strength of the smeared-up “open” pores is not sufficient to reliably maintain the number of pores below a critical number of “open” pores. Once the opening of more pores is initiated, more lubricant breakdowns occur and breakdown also severity increases (Figure 21). This results in wear phenomena, opening even more smeared up pores, which accelerates the increase in friction and temperature. Depending on the time sequence of this process, unstable, metastable, and stable operating behavior occurs. In case of polished–polished disk pairings, the operating behavior seems to be more stable because of the lower surface roughness.

In the optical measurements in Figure 16, an increasing surface porosity was observed even under good lubrication conditions. The surface porosity increased during the running time, without significant wear of the counter body. This again indicates that the mechanical strength of the smeared-up pores is not enough to reliably maintain the number of “open” pores below a critical number of “open” pores. Because of the high tribological stress, the smeared up pores could be opened in a normal direction because of the pressure gradient between the contact and porous structure.

## 6. Summary and Conclusions

Previous studies on the intrinsic self-lubrication of oil-impregnated sintered materials in highly-loaded rolling-sliding contacts indicated a strong influence of surface porosity on lubricant film formation and operating behavior. In order to understand these relationships, this study investigated the effects of surface porosity in detail.

Different surface porosity conditions were manufactured by grinding, polishing, and etch-polishing. Extensive documentation was conducted using a light microscope, scanning electron microscopy, and X-ray computed tomography. The operating behaviors of oil-impregnated sintered materials with different surface porosities were investigated at a twin-disk test rig. The influence of the local effects of the surface porosity on the lubricant film in the elastohydrodynamically lubricated (EHL) contacts was investigated at an optical tribometer based on thin film colorimetric interferometry.

The results show that a high surface porosity results in many lubricant film breakdowns, and, hence, in unstable operating behaviors. Thereby, “open” pores connected to the porous bulk structure of the test disks are much more serious than “closed” pores. A grinding process smears-up pores on the surface and allows stable operating behaviors because of an optimal number of pores, so that the lubricant can bleed and the film formation is not disturbed too much. However, the mechanical strength of this lower permeable layer is not sufficient to reliably maintain the number of pores below a critical number of “open” pores.

The findings demand an appropriate surface finish technique to manufacture a low permeable layer with adequate mechanical strength so as to improve the operating behavior of oil-impregnated sintered materials in highly-loaded contacts. Therefore, further work will investigate the adequate surface compaction techniques.

**Author Contributions:** Conceptualization, M.E., M.O., T.L. and P.S.; methodology, M.E., M.O. and T.L.; FZG experiments, M.E.; BUT experiments, M.O. and P.S.; formal analysis, T.L., I.K.; investigation, M.H. and B.-R.H.; writing—original draft preparation, M.E. and M.O.; writing—review and editing, T.L. and K.M.; supervision, M.H., B.-R.H. and K.S.; project administration, I.K., M.H., B.-R.H. and K.S.

**Funding:** We would like to thank the Deutsche Forschungsgemeinschaft (DFG, German Research Foundation, grant No. HO 1339/49-1), as well as the participating company, Miba, for their kind sponsorship of this research project. This work was further funded by the Czech Science Foundation (GACR), grant No. 18-26849J. Note that this research was initiated within the scientific cooperation between the Bavarian State Ministry of Education, Science, and the Arts, and the Ministry of Education, Youth, and Sports of the Czech Republic (project No. JC/14 Stahl; 8E15B011).

**Acknowledgments:** Special thanks go to Roman Látal and Raphael Köppl for performing the experiments on the optical tribometer.

**Conflicts of Interest:** The authors declare no conflict of interest. The funders had no role in the design of the study; in the collection, analyses, or interpretation of data; in the writing of the manuscript, or in the decision to publish the results.

## Nomenclature

$D$	Diameter of disk in mm
$E$	Young’s Modulus in N/mm <sup>2</sup>
$F_N$	Normal force in N
$F_R$	Friction force in N
$l_{eff}$	Disk width in mm
$L_t$	Measurement length in mm <sup>2</sup>
$p_H$	Hertzian pressure in N/mm <sup>2</sup>
$Ra$	Arithmetic mean roughness in $\mu\text{m}$
$V$	Volume in mm <sup>3</sup>
$v$	Velocity in m/s
$\Delta m$	Weight gain in g

$\theta_M$	Bulk temperature in °C
$\lambda_c$	Cut-off wavelength in mm
$\nu$	Poisson ratio
$\rho$	Density in g/cm <sup>3</sup>
$\Theta$	Volume based porosity in %
$\mu$	Coefficient of friction

#### Indices

1	Lower disk
2	Upper disk
g	Sliding
s	Solid
sf	Surface
$\Sigma$	Sum
CT	Measured by using X-ray computed tomography
$\Theta$	Porosity

## References

1. Dizdar, S. Pitting resistance of sintered small-module gears. *Proc. Inst. Mech. Eng. J* **2013**, *227*, 1225–1240. [\[CrossRef\]](#)
2. Lipp, K. Bericht Nr. FB-210: Oberflächenzerrüttung von Sinterstählen unter Konstanter und Veränderlicher Hertzscher Pressung mit Überlagerter Reibung (Schlupf) [Disruption of surface of sintered steel under constant and changing Hertzian pressure overlaid with friction (slip)]; Fraunhofer Institut für Betriebsfestigkeit LBF: Darmstadt, Germany, 1997.
3. Dlapka, M.; Danninger, H.; Gierl, C.; Lindqvist, B. Defining the pores in PM components. *Met. Powder Rep.* **2010**, *65*, 30–33. [\[CrossRef\]](#)
4. Kaneko, S.; Obara, S. Experimental investigation of mechanism of lubrication in porous journal bearings: part 1—observation of oil flow in porous matrix. *J. Tribol.* **1990**, *112*, 618–623. [\[CrossRef\]](#)
5. Pahl, W.; Goller, K. Self-lubricating bearings. *Tribol. Schmierungstech.* **2013**, *60*, 36–43.
6. Bartz, W.J.; Rübenbach, F. *Selbstschmierende und Wartungsfreie Gleitlager*, 1st ed.; Expert Verlag: Ehningen bei Böblingen, Germany, 1993; pp. 35–51. ISBN 978-381-690-957-6.
7. Matzner, A.; Macieszewski, A.; Franek, F. Limitations in sintered sliding bearings. *Tribol. Schmierungstech.* **1991**, *38*, 31–35.
8. Morgan, V.T.; Cameron, A. Mechanism of lubrication in porous metal bearings. In Proceedings of the 1957 Conference on Lubrication and Wear, London, UK, 1–3 October 1957; pp. 151–157.
9. Balasoiu, A.M.; Braun, M.J.; Modovan, S.I. A parametric study of a porous self-circulating hydrodynamic bearing. *Tribol. Int.* **2013**, *61*, 176–193. [\[CrossRef\]](#)
10. Scheichl, B.; Neacsu, I.A.; Kluwick, A. A novel view on lubricant flow undergoing cavitation in sintered journal bearings. *Tribol. Int.* **2015**, *88*, 189–209. [\[CrossRef\]](#)
11. Zhang, G.T.; Yin, Y.G.; Xue, L.; Zhu, G.Q.; Tian, M. Effects of surface roughness and porous structure on the hydrodynamic lubrication of multi-layer oil bearing. *Ind. Lubr. Tribol.* **2017**, *69*, 455–463. [\[CrossRef\]](#)
12. Fote, A.; Slade, A.R.; Feuerstein, S. The behavior of thin oil films in the presence of porous lubricant reservoirs. *Wear* **1978**, *46*, 377–385. [\[CrossRef\]](#)
13. Marchetti, M.; Meurisse, M.H.; Vergne, P.; Sicre, J.; Durand, M. Lubricant supply by porous reservoirs in space mechanisms. In Proceedings of the 26th Leeds-Lyon Symposium, Leeds, UK, 14–17 September 1999; pp. 777–786.
14. Marchetti, M.; Meurisse, M.H.; Vergne, P.; Sicre, J.; Durand, M. Analysis of oil supply phenomena by sintered porous reservoirs. *Tribol. Lett.* **2001**, *10*, 163–170. [\[CrossRef\]](#)
15. Li, X.; Sosa, M.; Olofsson, U. A pin-on-disc study of the tribology characteristics of sintered versus standard steel gear materials. *Wear* **2015**, *340–341*, 31–40. [\[CrossRef\]](#)
16. Li, X.; Olofsson, U. A study on friction and wear reduction due to porosity in powder metallurgic gear materials. *Tribol. Int.* **2017**, *110*, 86–95. [\[CrossRef\]](#)



17. Wedeven, L.D.; Cusano, C. Elastohydrodynamic film thickness measurements of artificially produced surface dents and grooves. *ASLE Trans.* **1979**, *22*, 369–381. [\[CrossRef\]](#)
18. Cusano, C.; Wedeven, L.D. Elastohydrodynamic film thickness measurements of artificially produced nonsmooth surfaces. *ASLE Trans.* **1981**, *24*, 1–14. [\[CrossRef\]](#)
19. Kaneta, M.; Kanada, T.; Nishikawa, H. Optical interferometric observations of the effects of a moving dent on point contact EHL. *Tribol. Ser.* **1997**, *32*, 69–79.
20. Kaneta, M.; Nishikawa, H. Experimental study on microelastohydrodynamic lubrication. *Proc. Inst. Mech. Eng. J* **1999**, *213*, 371–381. [\[CrossRef\]](#)
21. Mourier, L.; Mazuyer, D.; Lubrecht, A.A.; Donnet, C. Transient increase of film thickness in micro-textured EHL contacts. *Tribol. Int.* **2006**, *39*, 1745–1756. [\[CrossRef\]](#)
22. Mourier, L.; Mazuyer, D.; Ninove, F.P.; Lubrecht, A.A. Lubrication mechanisms with laser-surface-textured surfaces in elastohydrodynamic regime. *Proc. Inst. Mech. Eng. J.* **2010**, *224*, 697–711. [\[CrossRef\]](#)
23. Krupka, I.; Hartl, M. The effect of surface texturing on thin EHD lubrication films. *Tribol. Int.* **2007**, *40*, 1100–1110. [\[CrossRef\]](#)
24. Krupka, I.; Vrbka, M.; Hartl, M. Effect of surface texturing on mixed lubricated non-conformal contacts. *Tribol. Int.* **2008**, *41*, 1063–1073. [\[CrossRef\]](#)
25. Krupka, I.; Hartl, M. Effect of surface texturing on very thin film EHD lubricated contacts. *Tribol. Trans.* **2009**, *52*, 21–28. [\[CrossRef\]](#)
26. Frech, T.; Klocke, F.; Löpenhaus, C. Influence of the contact conditions in cold rolling on the density profile of PM gears. *Forsch. Ingenieurwesen* **2017**, *81*, 271–289. [\[CrossRef\]](#)
27. Sandner, C.; Ratzi, R.; Lorenz, B.; Tobie, T. Sintered gears—achievable load-carrying capacities by conventional and new production methods. In Proceedings of the International Conference on Gears, Munich, Germany, 13–15 March 2002; VDI-Report Nr. 1665. VDI-Verlag: Düsseldorf, Germany, 2002.
28. Yoshida, A.; Ohue, Y.; Karasuno, I. Comparison of surface durability & dynamic performance of powder metal & steel gears. In *Proceedings of the 1994 International Gearing Conference, Newcastle upon Tyne, UK, September 1994*; Mechanical Engineering Publications Ltd.: London, UK, 1994.
29. Ebner, M.; Lohner, T.; Michaelis, K.; Stemplinger, J.-P.; Höhn, B.-R.; Stahl, K. Self-lubricated elastohydrodynamic (EHL) contacts with oil-impregnated sintered materials. In Proceedings of the TAE Esslingen 20th International Colloquium, Stuttgart/Ostfildern, Germany, 28–30 January 2016.
30. Ebner, M.; Lohner, T.; Michaelis, K.; Höhn, B.-R.; Stahl, K. Self-lubricating gears with oil-impregnated sintered materials. *Forsch. Ingenieurwesen* **2017**, *81*, 175–190. [\[CrossRef\]](#)
31. Omasta, M.; Ebner, M.; Sperka, P.; Lohner, T.; Krupka, I.; Hartl, M.; Höhn, B.-R.; Stahl, K. Film formation in EHL contacts with oil-impregnated sintered materials. *Ind. Lubr. Tribol.* **2018**, *70*, 612–619. [\[CrossRef\]](#)
32. Michaelis, K. The integral temperature for evaluating the scuffing load capacity of cylindrical gear transmissions. Ph.D. Dissertation, Technical University of Munich, Munich, Germany, 1986.
33. Lohner, T.; Merz, R.; Mayer, J.; Michaelis, K.; Kopnarski, M.; Stahl, K. On the effect of plastic deformation (PD) additives in lubricants. *Tribol. Schmierungstech.* **2015**, *62*, 13–24.
34. Ebner, M.; Lohner, T.; Weigl, A.; Michaelis, K.; Stemplinger, J.-P.; Höhn, B.-R.; Stahl, K. Hochbelastete und schmierstoffgetränkte Wälzpaarungen aus Sintermaterial ohne externe Schmierstoffzuführung. *Tribol. Schmierungstech.* **2017**, *63*, 22–30.
35. Ebner, M.; Yilmaz, M.; Lohner, T.; Michaelis, K.; Höhn, B.-R.; Stahl, K. On the effect of starved lubrication on elastohydrodynamic (EHL) line contacts. *Tribol. Int.* **2018**, *118*, 515–523. [\[CrossRef\]](#)
36. MIBA. *Material Data Sheet of Sint-D31*; MIBA: Vorchdorf, Austria, 2014.
37. DIN. *DIN 30910—Teil 4: Sintermetall—Werkstoff-Leistungsdatenblätter (WLB)—Teil 4: Sintermetalle für Formteile*; Beuth Verlag: Berlin, Germany, 2010.
38. Deutsche Edelstahlwerke GmbH. *Materialdatenblatt für 1.7131/1.7139 (16MnCr5/16MnCrS5)*; Deutsche Edelstahlwerke GmbH: Witten, Germany, 2011.
39. Hartl, M.; Krupka, I.; Poliscuk, R.; Liska, M. An automatic system for real-time evaluation of EHD film thickness and shape based on the colorimetric interferometry. *Tribol. Trans.* **1999**, *42*, 303–309. [\[CrossRef\]](#)
40. Laukotka, E.M. *FVA-Heft Nr. 660—Referenzöle Datensammlung*; Forschungsvereinigung Antriebstechnik e.V.: Frankfurt/Main, Germany, 2007.

41. Emrich, S.; Lohner, T.; Ziegltrum, A.; Brodyanski, A.; Merz, R.; Stahl, K.; Kopnarski, M. Charakterisierung von triboinduzierten Schichten in Abhängigkeit des Schmierstoffs bei Verzahnungen. In Proceedings of the 57. Tribologie Fachtagung, Göttingen, Germany, 26–28 September 2016.
42. Zatočilová, A.; Zikmund, T.; Kaiser, J.; Paloušek, D.; Koutný, D. Measurement of the porosity of additive-manufactured Al-Cu alloy using x-ray computed tomography. *Solid State Phenom.* **2016**, *258*, 448–451. [[CrossRef](#)]
43. Greenwood, J.A.; Johnson, K.L. The behavior of transverse roughness in sliding elastohydrodynamically lubricated contacts. *Wear* **1992**, *153*, 107–117. [[CrossRef](#)]



© 2018 by the authors. Licensee MDPI, Basel, Switzerland. This article is an open access article distributed under the terms and conditions of the Creative Commons Attribution (CC BY) license (<http://creativecommons.org/licenses/by/4.0/>).